ACS APPLIED MATERIALS & INTERFACES

Research Article

www.acsami.org

Continuous Size Tuning of Monodispersed ZnO Nanoparticles and Its Size Effect on the Performance of Perovskite Solar Cells

Rong Zhang,[†,∥] Chengbin Fei,[†,∥] Bo Li,[‡] Haoyu Fu,[†] Jianjun Tian,*[,‡] and Guozhong Cao*[,†,§]

[†]Beijing Institute of Nanoenergy and Nanosystems, Chinese Academy of Sciences, National Center for Nanoscience and Technology (NCNST), Beijing 100083, China

[‡]Advanced Material and Technology Institute, University of Science and Technology, Beijing 100083, China

[§]Department of Materials Science and Engineering, University of Washington, Seattle, Washington 98195-2120, United States

Supporting Information

ABSTRACT: ZnO has been demonstrated to be a promising candidate to fabricate high efficiency perovskite solar cells (PSCs) in terms of its better electron extraction and transport properties. However, the inability of synthesis of ZnO nanoparticles (NPs) with minimal surface defects and agglomeration remains a great challenge hindering the fabrication of highly efficient PSCs. In this work, highly crystalline and agglomeration-free ZnO NPs with controlled size were synthesized through a facile solvothermal method. Such ZnO NPs were applied in the fabrication of meso-structured PSCs. The solar cells with ∼40 nm ZnO NPs exhibit the highest power conversion efficiency (PCE) of 15.92%. Steady-state and time-resolved photoluminescence measurements revealed the faster injection and lower charge recombination at the interface of ∼40 nm ZnO NPs and perovskite, resulting in significantly enhanced J_{SC} and V_{OC}.

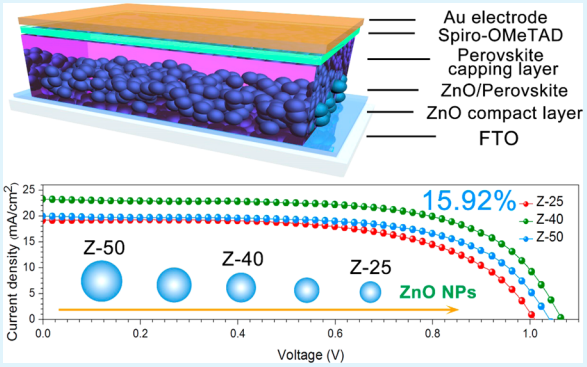

KEYWORDS: *ZnO nanoparticles, perovskite solar cells, monodisperse, size effect, electron transport*

INTRODUCTION

In the past few years, perovskite solar cells (PSCs) have attracted a lot of research effort worldwide, resulting in rapid progress in its power conversion efficiency with easy and low-cost solution-fabricating methods, thus exhibiting a great potential to compete with the traditional crystal Si-based solar cells.[1−3] In typical PSC devices, organic-metal hybrid halide perovskite (ABX_3) is used as the photoactive layer to absorb sunlight. For the most widely used $CH_3NH_3PbI_3$ ($MAPbI_3$), the bandgap is ∼1.50 eV, of which the absorption edge could reach ∼800 nm on the optical spectrum.[4,5] Through tuning the composition of the trihalide perovskite, such as the substitution of $CH_3NH_3^+$ (MA^+) with $NH_2CH{=}NH_2^+$ (FA^+), the bandgap could be easily altered, which is valuable for its use in tandem solar cells.[6] However, there are still many problems concerning the stability, toxicity, hysteresis, and carrier extraction efficiency,[7−10] preventing PSCs from widespread application and commercialization. So much work still needs to be done to attain better controlled properties of constituent materials and to enhance the performance of the solar cells by eliminating or controlling the above-mentioned shortcomings. From the point of view of carrier extraction efficiency, choosing an alternative electron transport layer with a lower conduction band and higher electron mobility may be an effective way to enhance the performance, like PCBM, SnO_2.[11−14]

TiO_2 has been most commonly employed as an ETL because of its suitable conduction band level when in contact with $MAPbI_3$ intrinsic layers, leading to fast electron injection from perovskite films to TiO_2 electron transport layers, but the transportation property of TiO_2 is less ideal, as the electron mobility of TiO_2 is just 0.1−4 $cm^2\ V\ s^{-1}$, resulting in high electron recombination.[15,16] ZnO is one of the most desired candidates as an electron-selective and transport material with slightly lower band position compared to TiO_2, and possesses a high electron mobility of 200−300 $cm^2\ V\ s^{-1}$ for bulk material and ∼1000 $cm^2\ V\ s^{-1}$ for single-crystal nanowires, which are several orders of magnitude larger than that of TiO_2.[17,18] Therefore, efficient extraction and transport of charge carriers from perovskite active layers to ZnO layers is expected. Until now, the efficiency of ZnO-based PSCs has exceeded 16% and various ZnO morphologies have been investigated as electron transport layer in PSCs.[19−21] However, there is little research on the effects of ZnO nanoparticles on electron−hole separation and transport in PSCs.[22,23] Nanostructured ZnO can be readily synthesized through various chemical processes, but the size tuning using a surfactant-free solution system has

Received: January 15, 2017
Accepted: February 28, 2017
Published: February 28, 2017

DOI: 10.1021/acsami.7b00726
ACS Appl. Mater. Interfaces 2017, 9, 9785−9794

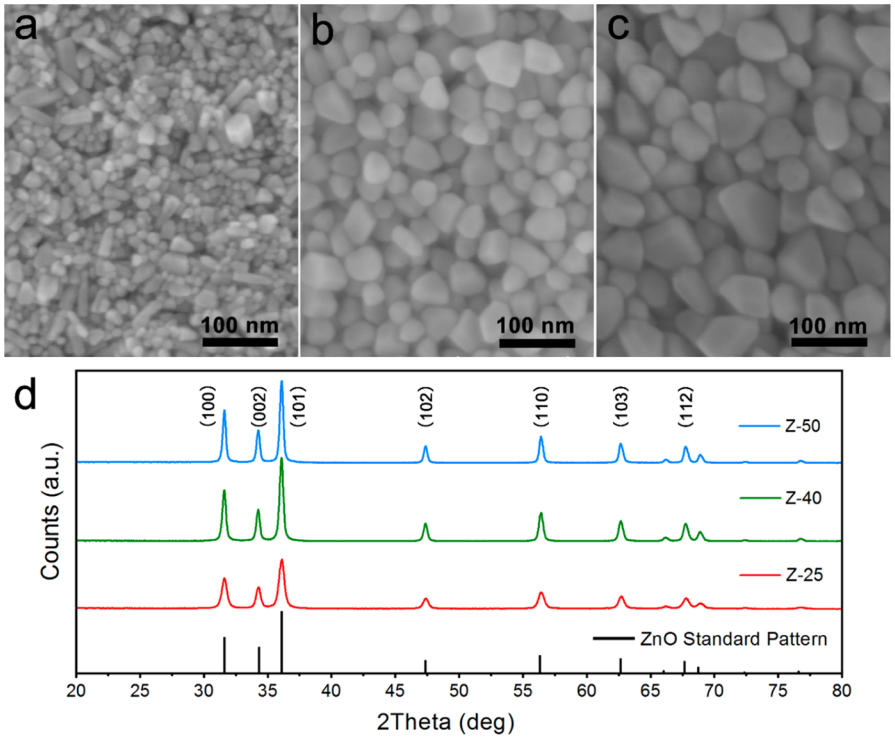

Figure 1. SEM images of various ZnO nanoparticles and their XRD pattern: (a) ~25 nm ZnO particles synthesized by methanol, (b) ~40 nm ZnO synthesized by ethanol, (c) ~50 nm ZnO synthesized by *n*-propanol; and (d) the XRD pattern of synthesized ZnO.

not been studied very much.[24,25] Although surfactant-free solution systems could avoid ion-doping, it could also lead to the easy agglomeration of ZnO particles, which is detrimental to the solar cell fabrication and performance. This is because the large sized ZnO particles coming from agglomeration would cause the direct contact of two carrier-selective layers taking account of the very thin perovskite films.[26] So the synthesis of well-dispersed ZnO nanoparticles with controlled size and without agglomeration is imperative for the further development of PSCs.

In this work, we synthesized ultrauniform ZnO NPs with different sizes through the solvothermal method and introduced ZnO NPs as an electron transport layer to replace the widely used TiO_2. By changing the synthesis solvents, we managed to control the ZnO NP sizes ranging from ~25 nm to ~50 nm. With assistance of the optical and electrochemical characterizations, the size effect of ZnO NPs on the performance of PSCs has been explicitly discussed. And finally we find that PSCs with ~40 nm ZnO NPs possess the highest efficiency of 15.92%.

EXPERIMENTAL SECTION

Synthesis of ZnO NPs Dispersions. 1.976 g Zinc acetate dihydrate was dissolved in 60 mL alcohols (~0.15 M), including absolute methanol, methanol/ethanol = 1:1, absolute ethanol, ethanol/*n*-propanol = 1:1, absolute *n*-propanol, then stirred for 30 min. Next, the solutions were transferred into a 100 mL teflon high pressure reactor, keeping at 150 °C for 12 h in furnace. After cooling down to room temperature, the supernatant was removed, and the precipitate was washed twice by ethanol. Finally, the ZnO precipitate was dispersed in 6 mL ethanol and 3 mL terpilenol to form the final ZnO precursors.

Fabrication of Electron Transport Layers. The commercial FTO glasses were etched by 2.5 M hydrochloric acid solution and zinc powder, then ultrasonically washed by distilled water, ethanol, and acetone sequentially. Next, the ZnO compact layers were deposited through magnetron sputtering at 100 W for 10 min and sintered under 350 °C for 30 min. After cooling down, 40 μL ZnO precursor was spin-coated at a speed of 2000 rpm for 3 s and 4000 rpm for 30 s on compact layers, similarly sintered at 350 °C for 30 min.

Fabrication of PSCs. All cell fabrication processes were conducted in a glovebox filled with N_2 atmosphere (O_2 and H_2O < 0.1 ppm). A modified two-step method was adopted to fabricate PSCs. First, 369.6 mg PbI_2 was dissolved in 665 uL dimethylformamide (DMF) and 135 mL dimethyl sulfoxide (DMSO), which was then heated at 70 °C for several hours to form the completely dissolved 1 M PbI_2 solution. The 30 mg/mL methylammonium iodide (MAI) solution was prepared by dissolving 120 mg MAI in 4 mL isopropanol. Next, 30 μL PbI_2 solution was dropped on mesoporous ZnO substrates that had been preheated at 70 °C, kept for 10 s to guarantee the full infiltration of PbI_2 solution into the mesoporous, then spin-coated at 4000 rpm for 30 s. Instantly, 150 μL MAI solution was added on PbI_2 films with a single flow, soaking for 60 s before spin-coating at 4000 rpm for 30 s to ensure the formation of $MAPbI_3$. The perovskite films were heated to 70 °C to transpire the solvents for 5 min. HTL layers were prepared by spin coating the spiro-OMeTAD solution as formerly reported at the speed of 4000 rpm for 30 s. Finally, Au was evaporated through thermal evaporator to form the back contact.

Characterizations of PSCs. Morphologies of ZnO nanoparticles were characterized by scanning electron microscope (SEM, Hitachi, SU-8020); A Shimadzu UV-3600 UV−vis−NIR spectrophotometer was used to measure the absorption and transmittance of mesoporous ZnO coated FTO glasses. *J*−*V* curves were obtained by an electrochemical workstation (Zahner, Zennium) under simulated AM 1.5 G illumination (100 mW/cm^2) provided by a solar simulator (Crowntech, SOL02 series), and all cells were masked by a metal aperture with active area of 0.07 cm^2. Before *J*−*V* curves test, devices were stored under dark conditions to prevent the light influence. The incident light intensity was calibrated with a NREL-calibrated Si solar cell. The photoluminescence (PL) spectra and fluorescence lifetime curves were carried out with combined steady state and time-resolved fluorescence spectrometer (Endinbergh, FLS920). The electro-

DOI: 10.1021/acsami.7b00726
ACS Appl. Mater. Interfaces 2017, 9, 9785−9794

chemical impedance spectroscopy (EIS) measurements were also performed with the electrochemical workstation.

RESULTS AND DISCUSSION

Continuous Size Tuning of ZnO Nanoparticles. Highly crystalline and homogeneous ZnO nanoparticles are synthesized through a facile solvothermal method. Figure 1a–c shows the scanning electron microscope (SEM) images of ZnO NPs, which are synthesized using methanol, ethanol, and *n*-propanol as solvent. In addition, mixtures of methanol/ethanol = 1:1(volume ratio) and ethanol/*n*-propanol = 1:1 have been used as well with the resulting ZnO nanoparticles shown in Figure S1 of the Supporting Information. The size of the resulting ZnO nanoparticles varies appreciably with the change of solvents from ~25 nm with methanol as solvent, to ~40 nm with ethanol, to ~50 nm with *n*-propanol, and the results are summarized in Table 1. The ZnO nanoparticles are denoted according to their particle sizes as Z-25, Z-40, and Z-50 for the sake of clarity and convenience. The XRD patterns are showed in Figure 1d. The high intensity and narrow width of the peaks are clear indicative of the well-crystallization of wurtzite ZnO NPs. The ZnO nanoparticle sizes are also estimated from the full-width of half-maximum of the XRD peaks using Scherer equation, and the results are also included in Table 1 and found to be in good agreement with the observation form SEM images.

Table 1. Particle Size Observed from SEM Image and Estimated from Scherer Equation

solvent	particle size (nm)	mark	fwhm (deg)	*D* (nm)
methanol	~25	Z-25	0.533	25.8
meth + eth	~30	Z-30	0.497	28.9
ethanol	~40	Z-40	0.346	40.1
eth + *n*-pro	~45	Z-45	0.322	44.8
n-propanol	~50	Z-50	0.305	48.1

In the synthesis process, ester elimination reactions are depicted as follows:[27]

$$Zn(CH_3COO)_2 + 2R{-}OH \rightarrow Zn(OH)_2 + 2R{-}OOCCH_3 \quad (1)$$

$$Zn(OH)_2 \rightarrow ZnO + H_2O \quad (2)$$

Despite the lack of hydroxide additives in the synthesis process, usually served as catalyst, the precursor complex $Zn(OH)_4^{2-}$ would form as reported since a small amount of bound water in the precursor, zinc acetate dihydrate.[28−30] Since all the chemicals and reaction conditions used in the synthesis of ZnO nanoparticles were kept the same, except that a different solvent was used, the significant variation of the size is likely to be ascribed to the different physical properties of the solvent. Table 2 summarizes the physical and chemical properties of the solvent used in this study: methanol, ethanol, and *n*-propanol.[31,32] Three solvents were very similar in acidity and dipole moment, which means that the pH condition and solubility of zinc acetate dihydrate in these solutions are likely to be similar. Appreciable differences, however, do exist in viscosity, dielectric constant, and the amount of hydroxyl groups per unit space. When methanol was used as a solvent, low viscosity would definitely promote the nucleation, the nucleation rate R_N could be described by the following:[33]

$$R_N = \frac{C_0 kT}{3\pi\lambda^3\eta} \exp\left(\frac{-\Delta G^*}{kT}\right) \quad (3)$$

where C_0, k, T, ΔG^*, λ, and η represent initial concentration, Boltzmann constant, temperature, nucleation energy barrier, diameter of growth species, and viscosity, respectively. It is also possible that a combination of large dielectric constant and high content of hydroxyl groups may further promote the nucleation with high nucleation density, resulting in the growth of small sized ZnO nanoparticles. The viscosity, dielectric constant, and content of hydroxyl groups would also affect the formation of a double layer and the zeta potential of the resulting ZnO nanoparticles, which in turn would control the subsequent crystal growth, Ostwald ripening, and possible agglomeration. The characterization of ZnO film porosity was necessary to prove that the pore filling would influence the performance of perovskite solar cells. As shown in Figure 2a,b, the N_2 adsorption−desorption isotherms and pore size distributions was measured for the porous density of ZnO powders (scrapped from the prepared thick films). With increased ZnO particle size from ~25 nm to ~40 nm and to ~50 nm, the specific surface area correspondingly decreased from 23.03 to 15.9, and to 13.8 m^2/g.

The synthesized ZnO NPs with sizes of 25−50 nm are dispersed in ethanol and terpilenol and then applied for the preparation of photoelectrodes. After being annealed at 350 °C for 30 min aiming to form coalescence between ZnO NPs,[34] the optical transmittance of ZnO nanoparticle coated FTO glasses were tested, and the results are presented in Figures 2c and S2. From the cross-sectional views, we clearly found the thickness discrepancy of all kinds of mesoporous layers are really tiny, thus the difference in transmittance is due to other factors. At the long-wave region of 380−800 nm, transmittance all exceeds 100%, which could be understood by the following equation according to the schema in Figure 2d:

$$100\% = \%\text{reflectance} + \%\text{transmitance} + \%\text{absorbance} \quad (4)$$

Normally, in UV−vis measurement, a baseline is needed to subtract the influence of the FTO glasses, but the coated ZnO NPs would flatten the rough surface of FTO glasses and reduce the back reflection, leading to the baseline offset, resulting in more transmission light through FTO layers. So the transmission over 100% is reasonable and good for the performance. In the case of short-wave region, the intense intrinsic absorption, corresponding to the energy bandgap (~3.3 eV), should be taken into account. Photoelectrodes with ~25 nm ZnO NPs show the strongest ultraviolet absorption, this could be precisely explained by the compactness of the mesoporous

Table 2. Physical and Chemical Properties of Methanol, Ethanol and *n*-Propanol

solvent	chemical formula	density (g/cm^3)	viscosity (mPa·s)	acidity (pK_a)	dielectric constants	dipole moment	hydroxyl per volume (mol/mL)
methanol	CH_3OH	0.792	0.545	15.5	32.7	1.70	0.025
ethanol	C_2H_5OH	0.789	1.2	15.9	24.5	1.69	0.017
n-propanol	C_3H_7OH	0.803	1.959	16	20.2	1.68	0.013

DOI: 10.1021/acsami.7b00726
ACS Appl. Mater. Interfaces 2017, 9, 9785−9794

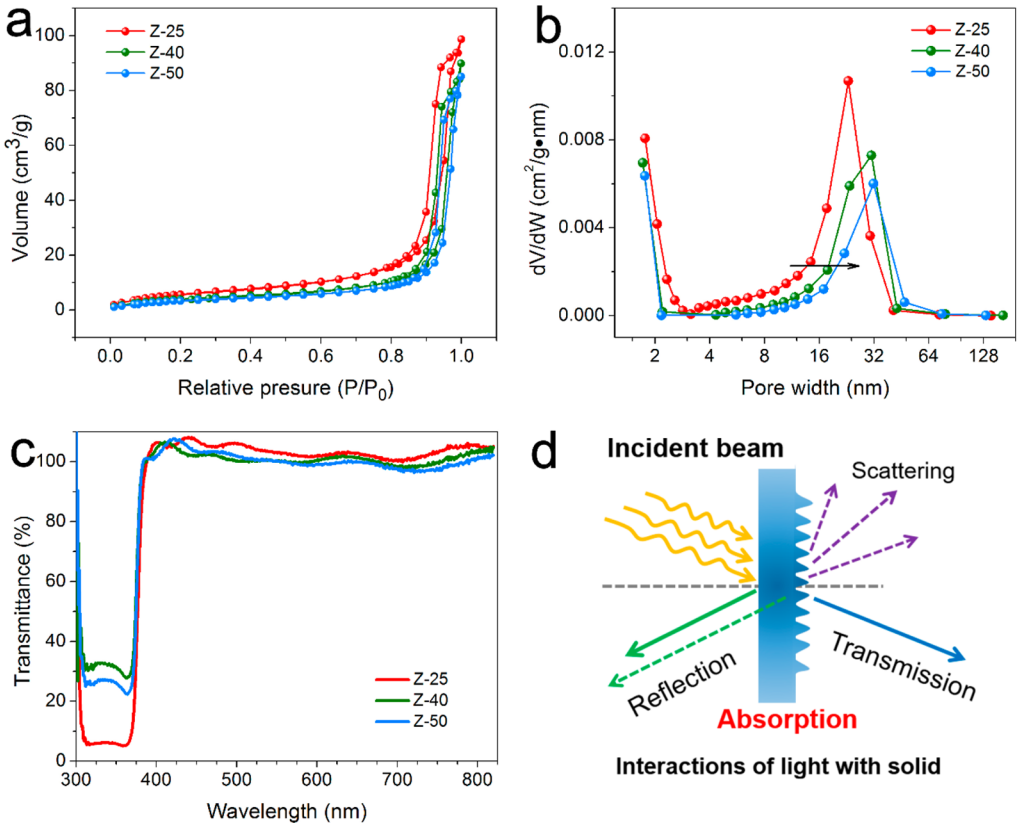

Figure 2. (a) N_2 adsorption−desorption isotherms and (b) pore size distributions of the three size ZnO NPs. (c) Transmittance measurements of mesoporous ZnO layers coated FTO glasses using different size ZnO NPs; and (d) illustration of interaction of light with solid.

layers. Smaller particles can form more dense mesoporous layers, which would enhance the absorption according to the Beer−Lambert Law. As for the small transmittance difference of photoelectrodes made by ∼40 nm and ∼50 nm ZnO NPs, we ascribe it to a scattering effect. It is well-known that the scattering effect of particles on light would be more serious if the particles sizes increase.[35] Hence, photoelectrodes made by ∼40 nm ZnO have a slightly larger transmittance in short-wave region.

Properties of Perovskite Films. As shown in Figure 3a, the ZnO NP substrates are applied for the fabrication of perovskite layers. To achieve better infiltration of perovskite, a modified sequential method is followed as the reported research.[36] After the formation of perovskite films, the devices are heated to 70 °C and kept for 5 min to transpire the solvents and promote the crystallinity given the the quick decomposition of perovskite films onto ZnO substrates.[37,38]

The morphologies of perovskite films on various substrates were obtained, as shown in Figure 3b−d, corresponding to ZnO NPs with sizes of ∼25, ∼40, ∼50 nm, respectively (Figure S3 shows the top views of ∼30 nm and ∼45 nm ZnO). Apparently, there is almost no variation in the top view morphologies of perovskite films with different substrates, no matter the coverage and the crystal size distributions. The XRD measurements are conducted as well, depicted in Figure 3e. Perovskite films on mesoporous ZnO substrates fabricated by small particles is lower in intensity compared to larger particles, which could be understood by that surface roughness and areas could have impacts on crystal growth of perovskite, which has been widely reported in the literature.[39−41] According to the Scherrer equation, grain size of the three kinds of perovskite films were ∼40 nm.

To further understand the optical performance of perovskite films based on various substrates, especially absorption and emission properties, the absorption and steady-state photoluminescence (PL) spectroscopy were measured. As shown in Figure 3f, perovskite films with large size ZnO NPs show higher absorption value, probably owing to the larger crystal grain formed in mesoporous structure, which is benefit for light harvesting. As for the normalized emission property, perovskite films on substrates made by ∼40 nm ZnO NPs own the lowest intensity compared to that of ∼25 nm and ∼50 nm ZnO NPs. The emission peaks are at ∼765 nm, originating from $MAPbI_3$. Lower intensity means less radiative recombination, that is to say more efficient electron transfer from perovskite films into ZnO mesoporous layers thinking of the slight difference of perovskite films,[20] proving that ∼40 nm size particles exhibit the best injection ability. Figure S5b was the comparison of perovskite films on Z-40 sample and bare glass, the drastic drop was clear, revealing the efficient charge transfer between ZnO and perovskite films.

Photovoltaic Properties of PSCs. Figure 4a−c demonstrates the cross sectional SEM images of PSCs based on different sized ZnO mesoporous substrates, where the thickness of the mesoporous ZnO layer, perovskite capping layers are approximately ∼350 and ∼300 nm, respectively (Figure S4 shows the cross section of PSCs fabricated by ∼30 nm and ∼45 nm ZnO, the thickness of each layer is almost the same). Visually, the infiltration of perovskite into mesoporous ZnO layers is not identical, mesoporous layer fabricated by ∼40 nm and ∼50 nm ZnO NPs have larger filling ratio compared to

DOI: 10.1021/acsami.7b00726
ACS Appl. Mater. Interfaces 2017, 9, 9785−9794

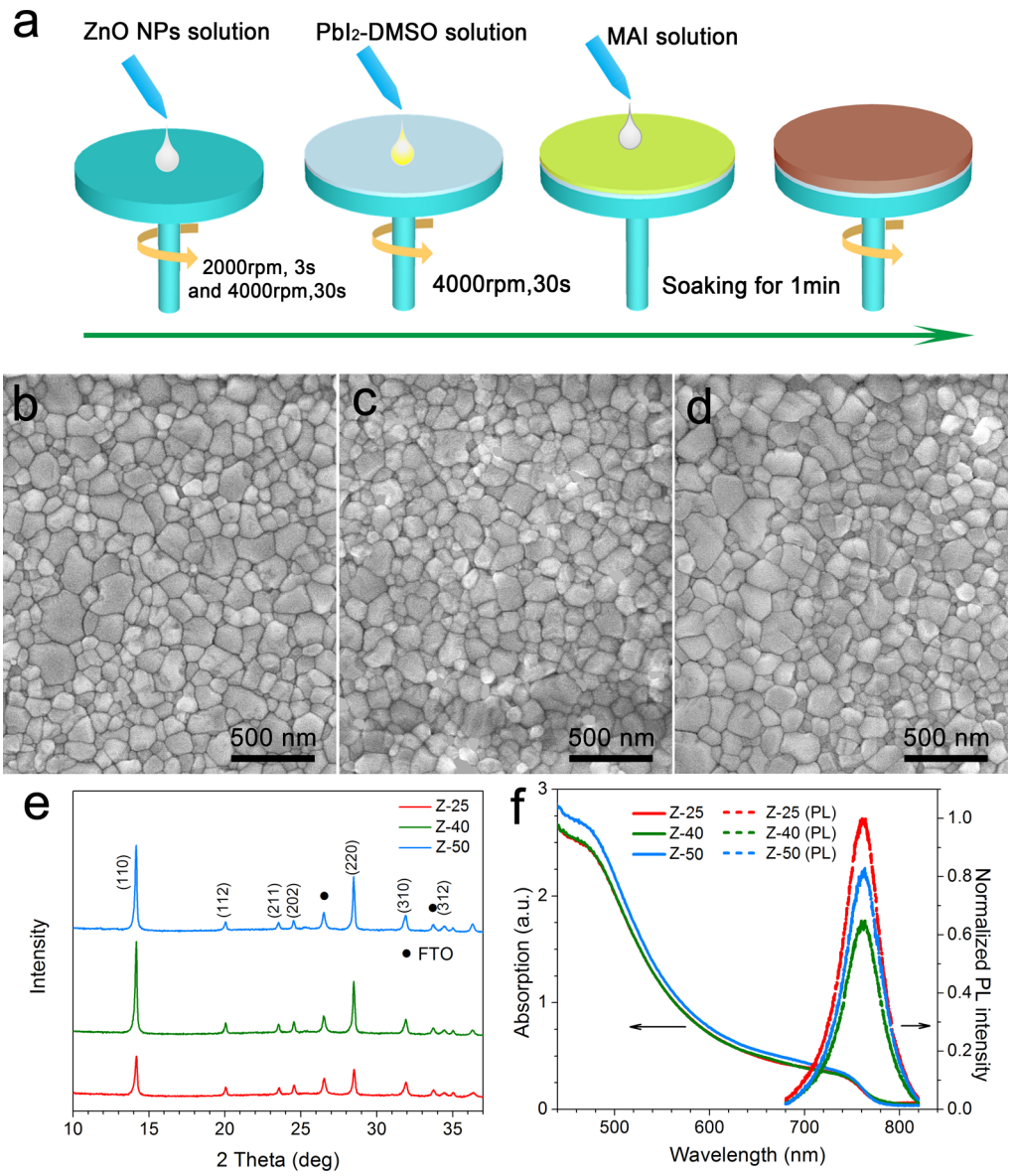

Figure 3. (a) Illustration of perovskite films fabrication process with modified sequential method; (b)-(d) Top views of perovskite layers fabricated on different size ZnO nanoparticles: ~ 25 nm, ~ 40 nm and ~50 nm; (e) XRD characterization of perovskite films on ZnO mesoporous layers; (f) Absorption spectrum and normalized steady-state photoluminescence spectrum (PL) of perovskite on different mesoporous ZnO substrates.

cells made by ~25 nm ZnO NPs, this could be attributed to the larger pores caused by large particles. Also, the EDX of the Z-40 and Z-50 sample were conducted to reveal the filling effect, but it is hard to distinguish the elemental difference at the very thin interface, shown as Figure S8.

Figure 4d illustrates the heterojunction structure PSCs. The mesoporous layers play a crucial part in extracting and transporting the photoexcited electrons from perovskite films to FTO electrodes. Generally, mesoporous layers fabricated by various ZnO NPs could introduce the following variables: surface area, pore size, and defects. Larger surface area would raise the contact area between ZnO and perovskite films, hence, the higher injection efficiency in PSCs with smaller particles will be within expectation, so in this respect, ~25 nm ZnO NPs would be more desirable.[42,43] However, the above results are not so. With the particle size decreasing, the formed pore size in the mesoporous layers will decrease as well, resulting in the poor infiltration of perovskite into mesoporous ZnO layers and eventually introducing lots of voids in mesoporous layers that is bad for cell performance. Besides, more grain boundaries and defects in the mesoporous layer also will increase as the surface areas increase, enhancing charge recombination. As a result, there is a balance between surface area, infiltration, and defects.

On the basis of above solar cell structure, photovoltaic properties of PSCs were measured under the scan speed of 100 mV/s from 1.2 V to −0.1 V and then back to 1.2 V. Figure 5a is the efficiency distribution diagram of 20 devices for each kind substrates. Clearly, devices based on ~40 nm ZnO nanoparticles showed better performance compared to the other two substrates. The $J-V$ curves of best performance PSCs based on various substrates are shown in Figure 5b (Figure S5a shows the $J-V$ curves including ~30 nm and ~45 nm ZnO based PSCs) and the detailed parameters are listed in Table 3. Among all devices, solar cells with ~40 nm ZnO NPs exhibit the highest efficiency of 15.92% with a short circuit current density (J_{SC}) of 23.26 mA/cm^2, an open circuit voltage (V_{OC}) of 1.06

DOI: 10.1021/acsami.7b00726
ACS Appl. Mater. Interfaces 2017, 9, 9785−9794

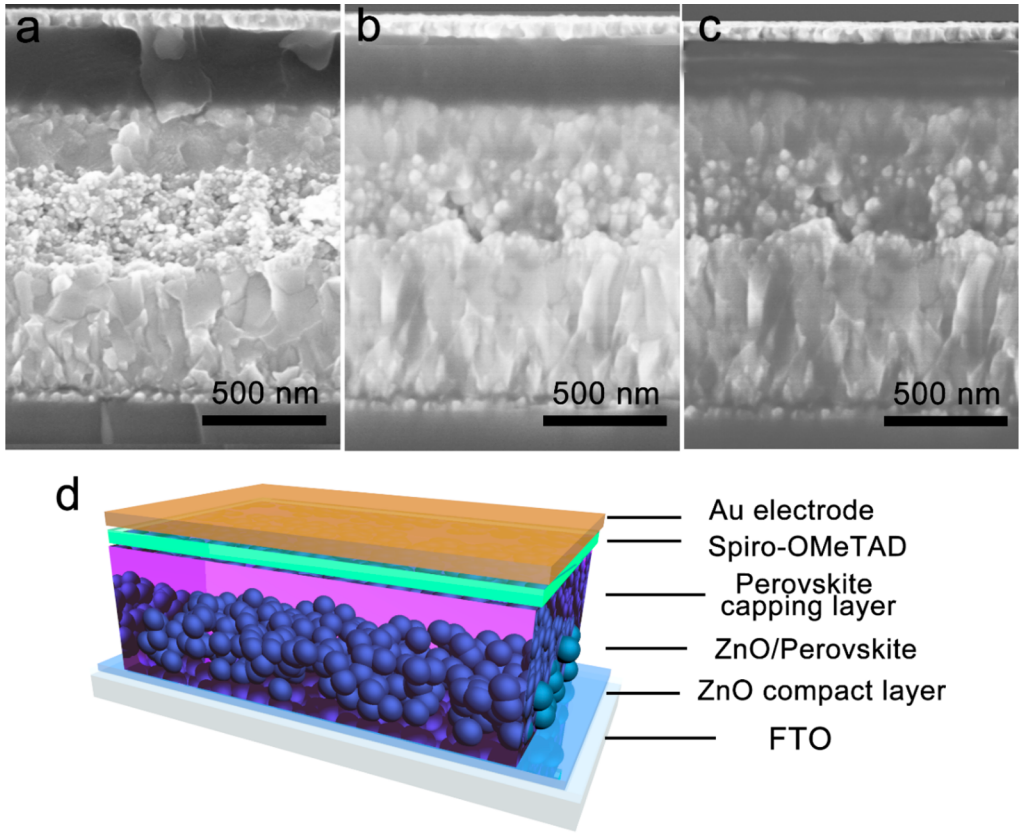

Figure 4. Cross sectional SEM images of the fabricated PSCs derived from various sized ZnO NPs: (a) ~25 nm, (b) ~40 nm, (c) ~50 nm; and (d) the schematic image of the mesoporous heterojunction PSCs.

V, and a fill factor (FF) of 0.64. With the increase of particle size from ~25 to ~40 nm, the J_{SC} shows a significant increase from 19.16 to 23.26 mA/cm^2. With further increas to ~50 nm, J_{SC} and V_{OC} decrease, and thus the PCE also declines to 13.20%.

To clearly reveal the dramatic improvement in current density, the incident photon-to-current conversion efficiency (IPCE) spectra measurement of various ZnO-based PSCs were conducted, as shown in Figure 5c. The IPCE of PSCs obtained from ~40 nm ZnO is higher than that of ~25 nm or ~50 nm ZnO NPs, which directly related to the variation of current density, corresponding to the integrated current density. The whole photon-to-current process consisted of three procedures: light harvesting, charge separation, and collection. Since the light harvesting efficiency has a positive correlation with the absorption value, the solar cells with different substrates show slightly different light harvesting according to the above UV−vis measurement results. So the J_{SC} difference originates from charge separation and collection efficiencies.

Due to the electron−hole separation at the interface of ETL and perovskite films, this would significantly strengthen the decay of fluorescence lifetime, the charge separation efficiency was qualitatively characterized by the time-resolved transient PL spectra (Figures 5d and S7a). The quenching of the transient PL intensity could be regarded from the following viewpoints: (1) the intrinsic radiative recombination of photoexcited electrons back to the ground state or (2) the extraction of ZnO electron selective layers and (3) the nonradiative recombination resulting from defects or boundaries. In principle, the radiative recombination takes place at a certain rate corresponding to materials properties. Thus, the faster or slower quenching of transient PL intensity can be derived from the extraction efficiency or the defect states in the interface of ZnO layers and perovskite films. Apparently, there still exists a contradiction with regard to carrier extraction, namely, the larger surface area not only promotes the electron extraction efficiency from perovskite films, but also increases the amount of defect states, and eventually causes a mesoporous layer with the intermediate ZnO NPs having the best performance. The lifetime decay curves could be simulated by a multiexponential decay model: τ_1 and τ_2, which commonly related to bimolecular recombination and free carriers recombination in the radiative channel, respectively.[44−46] From the fitting results listed in Table 3, perovskite films on ~40 nm ZnO NPs substrates display the shortest lifetime compared to the other two substrates, generally a short lifetime means a more efficient charge separation process, which is consistent with the steady-state test results that have been discussed above.

The electrical impedance spectroscopy (EIS) measurement has been conducted to elucidate the interface charge collection properties of PSCs based on various ZnO substrates under 0.8 V applied bias and dark conditions. Visually from Figure 5e (Figure S7b), the traditional front high frequency arc has disappeared, confirming that the interface contact capacitance (perovskite/ZnO or spiro-OMeTAD/Au) is nearly zero. To further understand the impedance spectra, the inset equivalent circuit is used to fit the test results to get detailed information, and the results are listed in Table 3. Generally, serial resistance R_S originates from two parts, one is the resistance of an external circuit such as the wires or FTO, the other is the resistance of the internal circuit like the transport resistance at electron or

DOI: 10.1021/acsami.7b00726
ACS Appl. Mater. Interfaces 2017, 9, 9785−9794

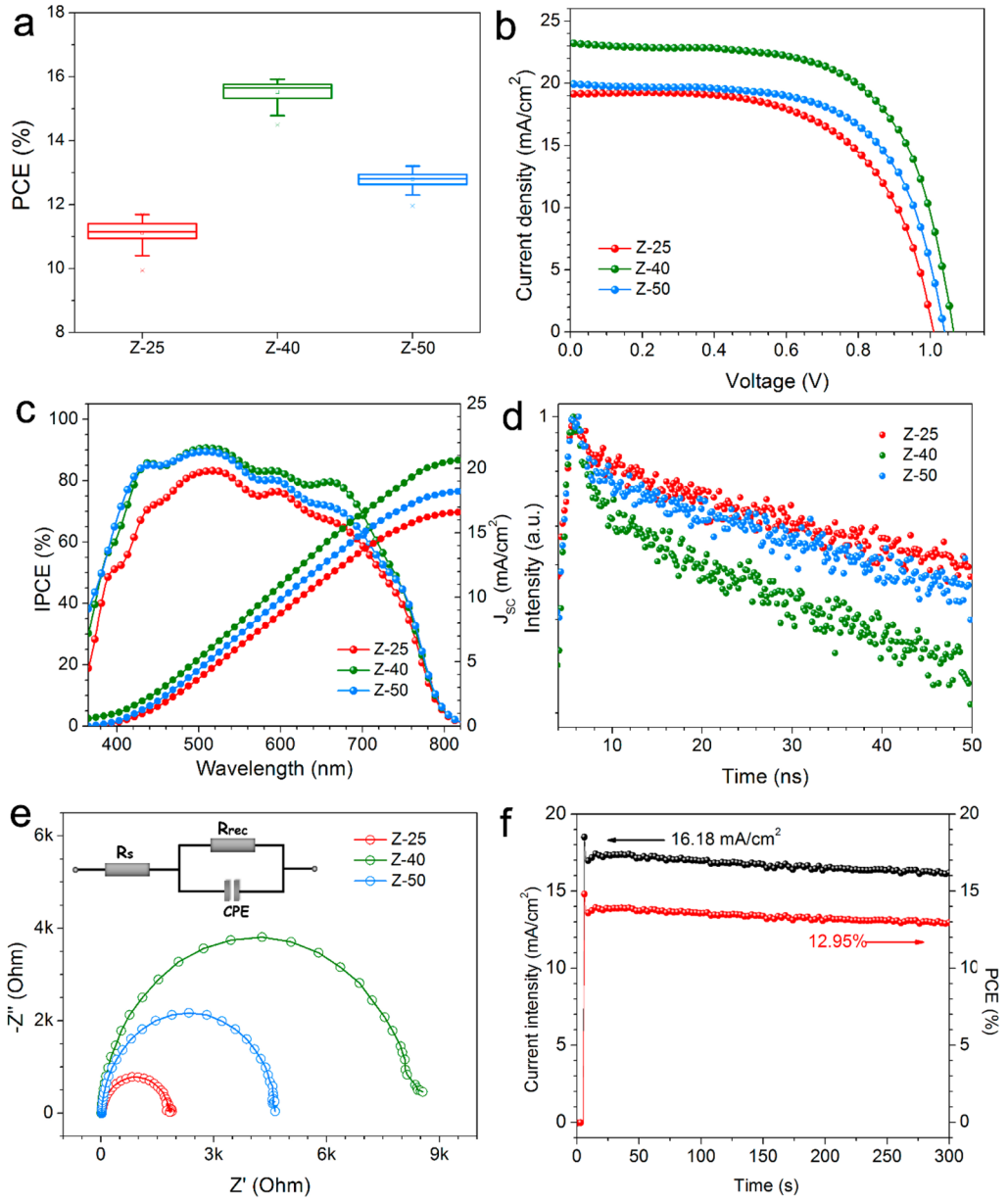

Figure 5. (a) The efficiency distribution diagram of PSCs based on different substrates; (b) J–V curves (scan speed: 100 mV/s) and (c) IPCE spectra and integrated current density of best performance device fabricated by various ZnO substrates; (d) time-resolved transient PL spectra of perovskite films on various ZnO mesoporous substrates; (e) the impedance spectra of all kinds of PSCs under 0.8 V applied bias in dark, the inset picture is the equivalent circuit; and (f) stable output at maximum point of PSCs based on ∼40 nm ZnO nanoparticles at bias of 0.8 V.

Table 3. Parameters of Current Density-Voltage Measurement, Electrochemical Impendence, and Transient PL Spectra of the PSCs that Based on Different Size ZnO Nanoparticle

PSCs	J_{SC} (mA/cm^2)	V_{OC} (V)	FF	PCE (%)	R_S (Ω)	R_{REC} (Ω)	τ_1 (ns)	τ_2 (ns)
Z-25	19.16	1.01	0.61	11.86	25	1280	2.04	55.95
Z-40	23.26	1.06	0.64	15.92	20	8550	1.50	36.14
Z-50	20.06	1.04	0.63	13.20	23	4650	1.98	51.98

hole selective layers and perovskite absorption layers.[47] Theoretically, as current passes through the interface of two materials, carriers would experience a resistive effect and with the increase of the interface area, the resistive effect would decrease with greater transportation channel. So in our case, the external condition is identical, the difference of R_S is ascribed to the internal circuit, more specifically, the ZnO/perovskite interface. As illustrated in Table 3, although the difference is minute, we can still detect the discrepancy of the ZnO/perovskite interface. The reduction of R_S when the particle size drops from ∼50 nm to ∼40 nm could be attributed to the decrease of interface area and the increase of R_S as the particles size further decrease to ∼25 nm is derived from the poor infiltration of perovskite into mesoporous ZnO layers, leading to the variation of V_{OC}.[48] Besides, the R_{REC} (recombination resistance) represents the charge recombination ability of PSCs.

DOI: 10.1021/acsami.7b00726
ACS Appl. Mater. Interfaces 2017, 9, 9785−9794

Clearly, PSCs fabricated by ~40 nm ZnO NPs possess the highest R_{REC}, verifying the highest J_{SC} of this kind devices.[49]

To further confirm the device reliability of PSCs based on ~40 nm ZnO nanoparticles, the stabilized photocurrent was measured at a constant bias of 0.8 V near the maximum power point as well and presented in Figure 5f, where a steady-state PCE of 12.95% is indicated. The discrepancy of the efficiency was ascribed to the hysteresis phenomenon caused by poor crystallinity of perovskite films when adopting ZnO as ETL. Poor crystallinity leads to a weak bond between ions and heavy ion migration happened. As reported in other literature, the ion migration and crystal defect in perovskite films will lead to a serious hysteresis phenomenon,[50,51] which could also be observed in our devices due to the limited annealing time (Figure S6a). ZnO particles were reported to damage perovskite due to the presence of hydroxyl groups on the surface, leading to the decreased long-term stability of the photovoltaic device.[52] The long-term stability of the solar cells (Z-40) was tested, and the measured results are presented in Figure S6b. The solar cells based on mesoporous ZnO were stored in dry air (the humidity was 10%) in the dark for 7 days retained over 95% of the initial PCE, demonstrating good stability.

CONCLUSIONS

High crystalline and ultrauniform ZnO nanoparticles without agglomeration were first synthesized by a simple solvothermal method. By choosing different solvents with varied viscosity, dielectric constants, and contents of hydroxyl groups, the size of ZnO nanoparticles was controlled and readily tunable from ~25 nm to ~50 nm. With these nanoparticles, mesoporous ZnO-based PSCs were fabricated. Through the characterizations on ZnO nanoparticles and PSCs, the influence of ZnO nanoparticles size variation on PSCs performance was believed to largely originate from the pore filling effect of perovskite into ZnO mesoporous, charge injection efficiency from the perovskite absorber to the ZnO layers, and the charge recombination ability. Therefore, the small size particles showed poor filling effect and heavy charge recombination, while large size particles demonstrated inadequate charge separation, thus the best performance was obtained with the intermediate ~40 nm ZnO nanoparticles. At last, the mesoporous ZnO based PSCs exhibited a high efficiency of 15.92%.

ASSOCIATED CONTENT

Supporting Information

The Supporting Information is available free of charge on the ACS Publications website at DOI: 10.1021/acsami.7b00726.

I–V, UV absorption, SEM images, and XRD pattern data of PSCs fabricated by ~30 nm and ~45 nm nanoparticles; and the hysteresis performance and stability measurement of best performance device (PDF)

AUTHOR INFORMATION

Corresponding Authors

*E-mail: tianjianjun@mater.ustb.edu.cn (J.J.T.).
*E-mail: gzcao@u.washington.edu (G.Z.C.).

ORCID

Jianjun Tian: 0000-0002-4008-0469
Guozhong Cao: 0000-0003-1498-4517

Author Contributions

‖These authors contributed equally to this work.

Notes

The authors declare no competing financial interest.

ACKNOWLEDGMENTS

This work was supported by the "thousands talents" program for pioneer researcher and his innovation team, China. This work was also supported by the National Science Foundation of China (51374029, 91433102), Program for New Century Excellent Talents in University (NCET-13-0668), Fundamental Research Funds for the Central Universities (FRF-TP-14-008C1), and China Postdoctoral Science Foundation (2014M550675).

REFERENCES

(1) Green, M. A.; Ho-Baillie, A.; Snaith, H. J. The Emergence of Perovskite Solar Cells. *Nat. Photonics* **2014**, *8* (7), 506–514.

(2) Docampo, P.; Ball, J. M.; Darwich, M.; Eperon, G. E.; Snaith, H. J. Efficient Organometal Trihalide Perovskite Planar-Heterojunction Solar Cells on Flexible Polymer Substrates. *Nat. Commun.* **2013**, *4*, 2761.

(3) Snaith, H. J. Perovskites: The Emergence of a New Era for Low-Cost, High-Efficiency Solar Cells. *J. Phys. Chem. Lett.* **2013**, *4* (21), 3623–3630.

(4) Li, B.; Tian, J.; Guo, L.; Fei, C.; Shen, T.; Qu, X.; Cao, G. Dynamic Growth of Pinhole-Free Conformal $CH_3NH_3PbI_3$ Film for Perovskite Solar Cells. *ACS Appl. Mater. Interfaces* **2016**, *8* (7), 4684–4690.

(5) Niu, G.; Li, W.; Li, J.; Wang, L. Progress of Interface Engineering in Perovskite Solar Cells. *Science China Materials* **2016**, *59* (9), 728–742.

(6) Pellet, N.; Gao, P.; Gregori, G.; Yang, T.-Y.; Nazeeruddin, M. K.; Maier, J.; Grätzel, M. Mixed-Organic-Cation Perovskite Photovoltaics for Enhanced Solar-Light Harvesting. *Angew. Chem., Int. Ed.* **2014**, *53* (12), 3151–3157.

(7) Leijtens, T.; Eperon, G. E.; Noel, N. K.; Habisreutinger, S. N.; Petrozza, A.; Snaith, H. J. Stability of Metal Halide Perovskite Solar Cells. *Adv. Energy Mater.* **2015**, *5* (20), 1500963.

(8) Zuo, C. T.; Bolink, H. J.; Han, H. W.; Huang, J. S.; Cahen, D.; Ding, L. M. Advances in Perovskite Solar Cells. *Adv. Sci.* **2016**, *3* (7), 1500324.

(9) Yang, G.; Tao, H.; Qin, P. L.; Ke, W. J.; Fang, G. J. Recent Progress in Electron Transport Layers for Efficient Perovskite Solar Cells. *J. Mater. Chem. A* **2016**, *4* (11), 3970–3990.

(10) Babayigit, A.; Ethirajan, A.; Muller, M.; Conings, B. Toxicity of Organometal Halide Perovskite Solar Cells. *Nat. Mater.* **2016**, *15* (3), 247–251.

(11) Chiang, C.-H.; Wu, C.-G. Bulk Heterojunction Perovskite–PCBM Solar Cells with High Fill Factor. *Nat. Photonics* **2016**, *10* (3), 196–200.

(12) Xu, X.; Zhang, H. Y.; Shi, J. J.; Dong, J.; Luo, Y. H.; Li, D. M.; Meng, Q. B. Highly Efficient Planar Perovskite Solar Cells with a TiO_2/ZnO Electron Transport Bilayer. *J. Mater. Chem. A* **2015**, *3* (38), 19288–19293.

(13) Baena, J. P. C.; Steier, L.; Tress, W.; Saliba, M.; Neutzner, S.; Matsui, T.; Giordano, F.; Jacobsson, T. J.; Kandada, A. R. S.; Zakeeruddin, S. M.; Petrozza, A.; Abate, A.; Nazeeruddin, M. K.; Gratzel, M.; Hagfeldt, A. Highly Efficient Planar Perovskite Solar Cells through Band Alignment Engineering. *Energy Environ. Sci.* **2015**, *8* (10), 2928–2934.

(14) Shen, T.; Tian, J.; Li, B.; Cao, G. Ultrathin ALD Coating on TiO_2 Photoanodes with Enhanced Quantum Dot Loading and Charge Collection in Quantum Dots Sensitized Solar Cells. *Science China Materials* **2016**, *59* (10), 833–841.

DOI: 10.1021/acsami.7b00726
ACS Appl. Mater. Interfaces 2017, 9, 9785–9794

(15) Zhu, L. Z.; Shao, Z. P.; Ye, J. J.; Zhang, X. H.; Pan, X.; Dai, S. Y. Mesoporous $BaSnO_3$ Layer Based Perovskite Solar Cells. *Chem. Commun.* **2016**, *52* (5), 970−973.
(16) Guo, L. X.; Fei, C. B.; Zhang, R.; Li, B.; Shen, T.; Tian, J. J.; Cao, G. Z. Impact of Sol Aging on TiO_2 Compact Layer and Photovoltaic Performance of Perovskite Solar Cell. *Sci. China-Mater.* **2016**, *59* (9), 710−718.
(17) Tian, J. J.; Zhang, Q. F.; Uchaker, E.; Gao, R.; Qu, X. H.; Zhang, S. E.; Cao, G. Z. Architectured ZnO Photoelectrode for High Efficiency Quantum Dot Sensitized Solar Cells. *Energy Environ. Sci.* **2013**, *6* (12), 3542−3547.
(18) Fei, C. B.; Tian, J. J.; Wang, Y. J.; Liu, X. G.; Lv, L. L.; Zhao, Z. X.; Cao, G. Z. Improved Charge Generation and Collection in Dye-Sensitized Solar Cells with Modified Photoanode Surface. *Nano Energy* **2014**, *10*, 353−362.
(19) Mahmood, K.; Swain, B. S.; Amassian, A. 16.1% Efficient Hysteresis-Free Mesostructured Perovskite Solar Cells Based on Synergistically Improved ZnO Nanorod Arrays. *Adv. Energy Mater.* **2015**, *5* (17), 1500568.
(20) You, J.; Meng, L.; Song, T. B.; Guo, T. F.; Yang, Y. M.; Chang, W. H.; Hong, Z.; Chen, H.; Zhou, H.; Chen, Q.; Liu, Y.; De Marco, N.; Yang, Y. Improved Air Stability of Perovskite Solar Cells via Solution-Processed Metal Oxide Transport Layers. *Nat. Nanotechnol.* **2015**, *11* (1), 75−81.
(21) Singh, M.; Rana, T. R.; Kim, S.; Kim, K.; Yun, J. H.; Kim, J. Silver Nanowires Binding with Sputtered ZnO to Fabricate Highly Conductive and Thermally Stable Transparent Electrode for Solar Cell Applications. *ACS Appl. Mater. Interfaces* **2016**, *8* (20), 12764−12771.
(22) Pascoe, A. R.; Yang, M. J.; Kopidakis, N.; Zhu, K.; Reese, M. O.; Rumbles, G.; Fekete, M.; Duffy, N. W.; Cheng, Y. B. Planar versus Mesoscopic Perovskite Microstructures: The Influence of $CH_3NH_3PbI_3$ Morphology on Charge Transport and Recombination Dynamics. *Nano Energy* **2016**, *22*, 439−452.
(23) Edri, E.; Kirmayer, S.; Henning, A.; Mukhopadhyay, S.; Gartsman, K.; Rosenwaks, Y.; Hodes, G.; Cahen, D. Why Lead Methylammonium Tri-Iodide Perovskite-Based Solar Cells Require a Mesoporous Electron Transporting Scaffold but Not Necessarily a Hole Conductor. *Nano Lett.* **2014**, *14* (2), 1000−1004.
(24) Zhang, Q. F.; Dandeneau, C. S.; Zhou, X. Y.; Cao, G. Z. ZnO Nanostructures for Dye-Sensitized Solar Cells. *Adv. Mater.* **2009**, *21* (41), 4087−4108.
(25) Janotti, A.; Van de Walle, C. G. Fundamentals of Zinc Oxide as a Semiconductor. *Rep. Prog. Phys.* **2009**, *72* (12), 126501.
(26) Pinna, N.; Niederberger, M. Surfactant-Free Nonaqueous Synthesis of Metal Oxide Nanostructures. *Angew. Chem., Int. Ed.* **2008**, *47* (29), 5292−5304.
(27) Djerdj, I.; Arcon, D.; Jaglicic, Z.; Niederberger, M. Nonaqueous Synthesis of Metal Oxide Nanoparticles: Short Review and Doped Titanium Dioxide as Case Study for the Preparation of Transition Metal-Doped Oxide Nanoparticles. *J. Solid State Chem.* **2008**, *181* (7), 1571−1581.
(28) Sakohara, S.; Ishida, M.; Anderson, M. A. Visible Luminescence and Surface Properties of Nanosized ZnO Colloids Prepared by Hydrolyzing Zinc Acetate. *J. Phys. Chem. B* **1998**, *102* (50), 10169−10175.
(29) Meulenkamp, E. A. Synthesis and Growth of ZnO Nanoparticles. *J. Phys. Chem. B* **1998**, *102* (29), 5566−5572.
(30) Haase, M.; Weller, H.; Henglein, A. Photochemistry and Radiation-Chemistry of Colloidal Semiconductors 0.23. Electron Storage on Zno Particles and Size Quantization. *J. Phys. Chem.* **1988**, *92* (2), 482−487.
(31) Mohsen-Nia, M.; Amiri, H.; Jazi, B. Dielectric Constants of Water, Methanol, Ethanol, Butanol and Acetone: Measurement and Computational Study. *J. Solution Chem.* **2010**, *39* (5), 701−708.
(32) Hassion, F. X.; Cole, R. H. Dielectric Properties of Liquid Ethanol and 2-Propanol. *J. Chem. Phys.* **1955**, *23* (10), 1756−1761.
(33) Kim, Y. T.; Park, J.; Kim, S.; Park, D. W.; Choi, J. Fabrication of Hierarchical ZnO Nanostructures for Dye-Sensitized Solar Cells. *Electrochim. Acta* **2012**, *78*, 417−421.
(34) Park, K.; Zhang, Q. F.; Garcia, B. B.; Cao, G. Z. Effect of Annealing Temperature on TiO_2-ZnO Core-Shell Aggregate Photoelectrodes of Dye-Sensitized Solar Cells. *J. Phys. Chem. C* **2011**, *115* (11), 4927−4934.
(35) Zhang, Q. F.; Chou, T. P.; Russo, B.; Jenekhe, S. A.; Cao, G. Polydisperse Aggregates of ZnO Nanocrystallites: A Method for Energy-Conversion-Efficiency Enhancement in Dye-Sensitized Solar Cells. *Adv. Funct. Mater.* **2008**, *18* (11), 1654−1660.
(36) Li, W. Z.; Fan, J. D.; Li, J. W.; Mai, Y. H.; Wang, L. D. Controllable Grain Morphology of Perovskite Absorber Film by Molecular Self-Assembly toward Efficient Solar Cell Exceeding 17%. *J. Am. Chem. Soc.* **2015**, *137* (32), 10399−10405.
(37) Yang, J. L.; Siempelkamp, B. D.; Mosconi, E.; De Angelis, F.; Kelly, T. L. Origin of the Thermal Instability in $CH_3NH_3PbI_3$ Thin Films Deposited on ZnO. *Chem. Mater.* **2015**, *27* (12), 4229−4236.
(38) Cheng, Y. H.; Yang, Q. D.; Xiao, J. Y.; Xue, Q. F.; Li, H. W.; Guan, Z. Q.; Yip, H. L.; Tsang, S. W. Decomposition of Organometal Halide Perovskite Films on Zinc Oxide Nanoparticles. *ACS Appl. Mater. Interfaces* **2015**, *7* (36), 19986−19993.
(39) Liang, Z. Q.; Zhang, Q. F.; Wiranwetchayan, O.; Xi, J. T.; Yang, Z.; Park, K.; Li, C. D.; Cao, G. Z. Effects of the Morphology of a ZnO Buffer Layer on the Photovoltaic Performance of Inverted Polymer Solar Cells. *Adv. Funct. Mater.* **2012**, *22* (10), 2194−2201.
(40) Sung, S. D.; Ojha, D. P.; You, J. S.; Lee, J.; Kim, J.; Lee, W. I. 50 nm Sized Spherical TiO_2 Nanocrystals for Highly Efficient Mesoscopic Perovskite Solar Cells. *Nanoscale* **2015**, *7* (19), 8898−8906.
(41) Jeon, N. J.; Noh, J. H.; Kim, Y. C.; Yang, W. S.; Ryu, S.; Il Seol, S. Solvent Engineering for High-Performance Inorganic-Organic Hybrid Perovskite Solar Cells. *Nat. Mater.* **2014**, *13* (9), 897−903.
(42) Chou, T. P.; Zhang, Q. F.; Cao, G. Z. Effects of Dye Loading Conditions on the Energy Conversion Efficiency of ZnO and TiO_2 Dye-Sensitized Solar Cells. *J. Phys. Chem. C* **2007**, *111* (50), 18804−18811.
(43) Chou, T. P.; Zhang, Q. F.; Russo, B.; Fryxell, G. E.; Cao, G. Z. Titania Particle Size Effect on the Overall Performance of Dye-Sensitized Solar Cells. *J. Phys. Chem. C* **2007**, *111* (17), 6296−6302.
(44) Zhao, Z. X.; Chen, X. Y.; Wu, H. Q.; Wu, X. M.; Cao, G. Z. Probing the Photovoltage and Photocurrent in Perovskite Solar Cells with Nanoscale Resolution. *Adv. Funct. Mater.* **2016**, *26* (18), 3048−3058.
(45) Ohnesorge, B.; Weigand, R.; Bacher, G.; Forchel, A.; Riedl, W.; Karg, F. H. Minority-Carrier Lifetime and Efficiency of $Cu(In,Ga)Se_2$ Solar Cells. *Appl. Phys. Lett.* **1998**, *73* (9), 1224−1226.
(46) Chen, Q.; Zhou, H. P.; Song, T. B.; Luo, S.; Hong, Z. R.; Duan, H. S.; Dou, L. T.; Liu, Y. S.; Yang, Y. Controllable Self-Induced Passivation of Hybrid Lead Iodide Perovskites toward High Performance Solar Cells. *Nano Lett.* **2014**, *14* (7), 4158−4163.
(47) Juarez-Perez, E. J.; Wussler, M.; Fabregat-Santiago, F.; Lakus-Wollny, K.; Mankel, E.; Mayer, T.; Jaegermann, W.; Mora-Sero, I. Role of the Selective Contacts in the Performance of Lead Halide Perovskite Solar Cells. *J. Phys. Chem. Lett.* **2014**, *5* (4), 680−685.
(48) Bisquert, J.; Bertoluzzi, L.; Mora-Sero, I.; Garcia-Belmonte, G. Theory of Impedance and Capacitance Spectroscopy of Solar Cells with Dielectric Relaxation, Drift-Diffusion Transport, and Recombination. *J. Phys. Chem. C* **2014**, *118* (33), 18983−18991.
(49) Suarez, B.; Gonzalez-Pedro, V.; Ripolles, T. S.; Sanchez, R. S.; Otero, L.; Mora-Sero, I. Recombination Study of Combined Halides (Cl, Br, I) Perovskite Solar Cells. *J. Phys. Chem. Lett.* **2014**, *5* (10), 1628−1635.
(50) Zhao, Y.; Liang, C. J.; Zhang, H. M.; Li, D.; Tian, D.; Li, G. B.; Jing, X. P.; Zhang, W. G.; Xiao, W. K.; Liu, Q.; Zhang, F. J.; He, Z. Q. Anomalously Large Interface Charge in Polarity-Switchable Photovoltaic Devices: an Indication of Mobile Ions in Organic-Inorganic Halide Perovskites. *Energy Environ. Sci.* **2015**, *8* (4), 1256−1260.
(51) Eames, C.; Frost, J. M.; Barnes, P. R. F.; O'Regan, B. C.; Walsh, A.; Islam, M. S. Ionic Transport in Hybrid Lead Iodide Perovskite Solar Cells. *Nat. Commun.* **2015**, *6*, 7497.
(52) Wang, P.; Zhao, J. J.; Liu, J. X.; Wei, L. Y.; Liu, Z. H.; Guan, L. H.; Cao, G. Z. Stabilization of Organometal Halide Perovskite Films

DOI: 10.1021/acsami.7b00726
ACS Appl. Mater. Interfaces 2017, 9, 9785−9794

by SnO_2 Coating with Inactive Surface Hydroxyl Groups on ZnO Nanorods. *J. Power Sources* **2017**, *339*, 51−60.

DOI: 10.1021/acsami.7b00726
ACS Appl. Mater. Interfaces 2017, 9, 9785−9794